



저작자표시-비영리-변경금지 2.0 대한민국

이용자는 아래의 조건을 따르는 경우에 한하여 자유롭게

- 이 저작물을 복제, 배포, 전송, 전시, 공연 및 방송할 수 있습니다.

다음과 같은 조건을 따라야 합니다:



저작자표시. 귀하는 원저작자를 표시하여야 합니다.



비영리. 귀하는 이 저작물을 영리 목적으로 이용할 수 없습니다.



변경금지. 귀하는 이 저작물을 개작, 변형 또는 가공할 수 없습니다.

- 귀하는, 이 저작물의 재이용이나 배포의 경우, 이 저작물에 적용된 이용허락조건을 명확하게 나타내어야 합니다.
- 저작권자로부터 별도의 허가를 받으면 이러한 조건들은 적용되지 않습니다.

저작권법에 따른 이용자의 권리는 위의 내용에 의하여 영향을 받지 않습니다.

이것은 [이용허락규약\(Legal Code\)](#)을 이해하기 쉽게 요약한 것입니다.

[Disclaimer](#)

공학석사학위논문

레이저 펄스 에너지가 레이저 유도 기포
거동에 미치는 효과: 경계선에서 먼 경우

Effects of Laser Pulse Energy on Laser Induced
Bubble Behavior: Far from Boundaries Case

2018년 8월

서울대학교 대학원

기계항공공학부

신 재 건

Effects of Laser Pulse Energy on Laser Induced Bubble Behavior: Far from Boundaries Case

Jaegun Shin

Mechanical and Aerospace Engineering

College of Engineering

Seoul National University

Abstract

To investigate cavitation bubble behavior far from boundaries, pulsed laser has been used to generate a single bubble. From high energy density of a pulsed laser, focusing it easily overcomes the optical breakdown threshold of water. The plasma is locally generated at and near the focusing point, and rapidly cools down to turn water into vapor. Varying laser pulse energy, bubble has been produced far from the boundaries, and the time-series behavior has been taken by the Schlieren imaging technique, which enables accurate boundary extraction from image processing. At 30mJ of laser pulse energy, bubble goes through the following: expansion, collapse, rebound, collapse, rebound and water jet formation, and final collapse. However, at 42.6mJ, the bubble expands, collapses then rebounds with water jet, and finally collapses.

Keyword : Pulsed laser, Cavitation, Surface tension, Hydrostatic force, Weber number, Bond number

Student Number : 2016-20692

Table of Contents

Chapter 1. Introduction.....	1
1.1 Background.....	1
1.2 Laser induced cavitation.....	5
Chapter 2. Scope of Study	7
2.1 Previous research.....	7
2.2 Research objectives.....	9
Chapter 3. Experimental setup	11
3.1 Setup overview	11
3.2 Bubble generation	12
3.3 Schlieren imaging.....	21
3.4 Energy control	26
3.5 Time delay control.....	27
Chapter 4. Results	30
4.1 Energy measurements.....	30
4.2 Bubble behaviors.....	32
4.3 Discussion: Difference in bubble behaviors	35
Chapter 5. Conclusions	43
Bibliography	44

List of Figures

Fig. 1.1 Diagram of bubble growth.....	2
Fig. 1.2 Spark induced bubble	4
Fig. 1.3 Laser induced cavitation–dissociation of water molecules.....	6
Fig. 3.1 Experimental setup	11
Fig. 3.2 Beam divergence	14
Fig. 3.3 Keplerian type beam expander.....	18
Fig. 3.4 Galilean type beam expander	18
Fig. 3.5 Role of iris	20
Fig. 3.6 Camera lens schematic	24
Fig. 3.7 Beam polarity with a wave palte	27
Fig. 3.8 Beam polarity after rotation of wave plate	27
Fig. 3.9 Time domain control	29
Fig. 4.1 Energy measurements	31
Fig. 4.2 Schlieren images at 30mJ	33
Fig. 4.3 Schlieren images at 42.6mJ	34
Fig. 4.4 Normalized bubble radius.....	36
Fig. 4.5 Bubble shape before first collapse(10 microseconds)	39
Fig. 4.6 Energy partition for both cases.....	40

Nomenclature

E_{bubble} : Bubble energy

f : Focus length

F : Force

m : Jet mass

$P_{Ambient}$: Ambient pressure

P_{Gas} : Non-condensable gas pressure

P_{Vapor} : Vapor pressure

P_{∞} : Pressure at ∞

R : Radius of bubble

R_{max} : Maximum radius

$R_{max,rebound}$: Maximum radius at rebound

\dot{R} : Time derivative of R

\ddot{R} : Time derivative of \dot{R}

$R(t)$: Radius at time t

$S(t)$: Surface of bubble at time t

t : Time

v : Spatially averaged jet velocity

$V_{jet,max}$: Maximum jet volume

V_{nor} : Normalized jet volume

$|\nabla p|$: Absolute magnitude of pressure gradient

γ : Surface tension

φ : Conversion angle between Cartesian and polar coordinate

θ : Polar angle

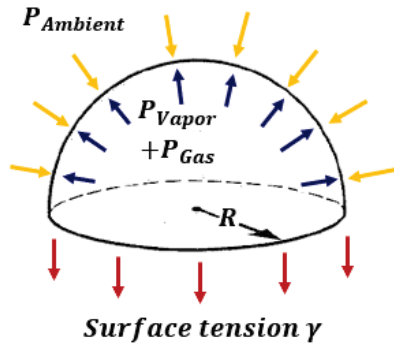
ρ : Liquid density

Chapter 1. Introduction

1.1. Background

Cavitation research has started from cavitation inside the hydraulic machineries. To enhance performance, pumps and hydraulic turbines have been forced to rotate faster as time passed. High speed resulted in low local pressure which becomes lower than the vapor pressure. Vapor pressure is the pressure of the molecules to condense and evaporate at the same rate, which is in dynamic equilibrium. To be more precise, the term vapor pressure here means saturated vapor pressure at given temperature and pressure. If the local pressure becomes lower than the vapor pressure, rate of evaporation becomes dominant, and phase change occurs drastically. Therefore, the move toward faster rotation caused in serious cavitation in rotating machines and resulted in performance degradation, loss in efficiency, noise and even hydraulic instabilities[1].

Cavitation in hydraulic machineries is called hydrodynamic cavitation. From the diagram shown in Fig. 1.1, vapor pressure, non-condensable gas pressure tend to expand the bubble, whereas liquid pressure and surface tension act to suppress the bubble growth. If the condition confines liquid pressure at constant, surface tension becomes the key component in



**Assuming equilibrium,
Force balance :**

$$P_{Ambient} = P_{Gas} + P_{Vapor} - \frac{2\gamma}{R}$$

Fig. 1.1 Diagram of bubble growth

occurrence of hydrodynamic cavitation. From the energy point of view to explain the hydrodynamic cavitation, external kinetic energy from the rotating impeller excites the molecules to overcome the surface energy, which is from the intermolecular forces between water molecules.

Intermolecular force is limited to short distance and thus the surface tension is the averaged value that represent it. Therefore, considering the localized occurrence in hydrodynamic cavitation, accurate estimation, measurement, and prediction of surface tension is highly challenging. Present available surface tension values are all from measurement under quasi-steady condition, with water-water or water-air interfaces. Fast moving condition makes it even difficult to quantify. Other parameters such as non-condensable gas and vapor pressure are not only non-uniform, but also highly unsteady in nature. Non-condensable gas comes from diffused gas inside water, and the amount of

diffusivity is dependent on many parameters, such as temperature, salinity, PH, and more. Current measurement methodology enables the quantification of dissolved gas content for specific gases in ppb. However, the measurement is from optical reflectivity, and is the averaged value. Vapor pressure was coming from the interfacial diffusion, and with surface tension, is hard to quantify.

The difficulties in accurate estimation, measurement, and possible prediction in hydrodynamic cavitation made fundamental cavitation research difficult. The variables are non-uniform, making control of location, extent and rate impossible. In hydrodynamic cavitation which usually occurs on impeller blade cavitation takes the form of cloud. Many bubbles are concentrated on localized area and interact with surrounding water and structure. Investigating such cloud behavior is difficult, since not only bubble-liquid interaction is happening, but also bubble-bubble interaction becomes also significant. For these reasons, many researchers turned to single bubble behavior and tried to explain cloud behavior. However, making a single bubble repeatedly and coherently was almost impossible using hydrodynamic cavitation, and such difficulties gave immediate rise to other methods of creating a single bubble.

To overcome intermolecular forces, external energy had to be focused into a single point to create a bubble on demand. Early method was to use electrodes. A pair of plus and minus electrodes with few millimeters apart were put into water and short current was shot to generate electric spark (Fig. 1.2). The spark which is at plasma state, was rapidly quenched by outside water and turned into vapor. There are many previous papers regarding the method and the resultant bubble was well

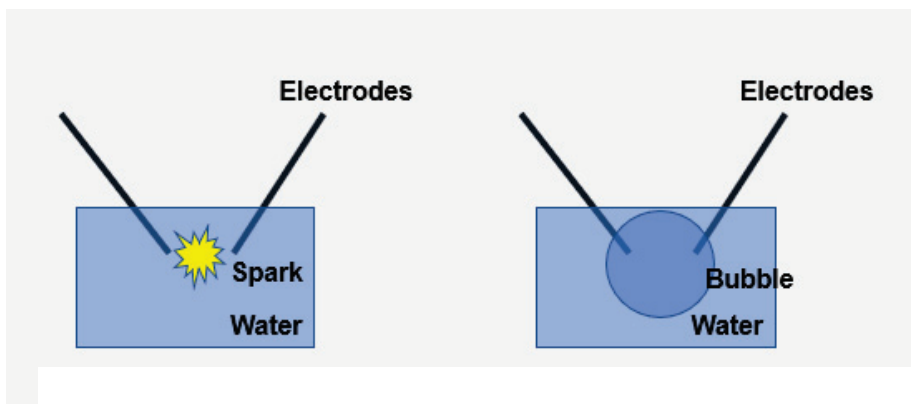


Fig. 1.2 Spark induced bubble

described by the Rayleigh equation [2]. However, Rayleigh solution only provides initial growth and collapse phase and the remaining bubble behavior until final diffusion has been known to be affected by the external confinements. In case of spark generated bubble, the electrodes can alter the bubble behavior, and thus the precise control of energy would not create very repeatable and coherent bubble.

Acoustic cavitation, which occurs from high frequency

tension points, is also one form of such energy deposition methods. The bubbles are generated in cloud, and exciting frequency is higher than the bubble lifetime frequency. Therefore, single bubble cannot be captured and the lifetime of a single bubble is driven by the external trigger, and thus not applied in the present study.

1.2. Laser induced cavitation

More recently, laser technology has been developed and has been improving rapidly. One of the lasers that has been introduced is a nanosecond pulsed laser. Unlike continuous laser(CW), the pulse has a pulse width of few nanoseconds and generates a peak power of order of megawatts. This high peak power easily overcomes the optical breakdown threshold of water, and water molecules are dissociated into ionized particles such as H^+ , O^+ , OH^+ and electrons. Not only hydrogen bonds that generate a surface tension breaks down, but also covalent bonds that sustain water molecules are dissociated(Fig. 1.3). From the spectrum analysis during plasma emission, such dissociation has been confirmed and electron density has also been measured. The plasma state does not last for long, and after a laser shot, plasma formation occurs almost instantaneously and from surrounding cool water, it is cooled down rapidly. Since the external energy is not supplied after a laser shot, plasma state

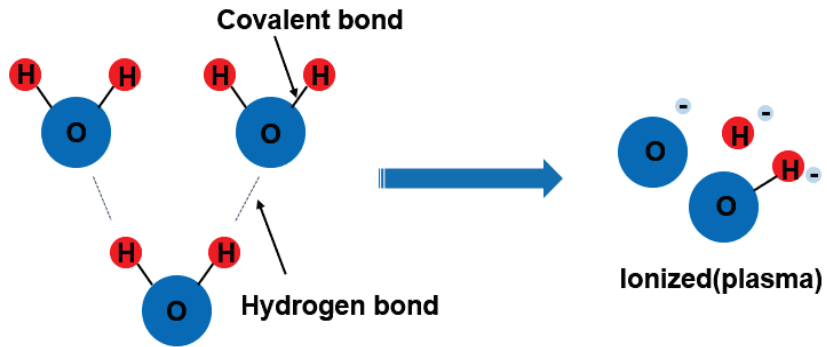


Fig. 1.3 Laser induced cavitation – dissociation of water molecules

turns into vapor state. The bubble is now seen and can be captured. The duration of plasma state is known to be about few hundred nanoseconds and after recombined into vapor, bubble lifetime begins [3].

The advantage of laser induced cavitation over spark generated bubbles is that using laser is virtually non-intrusive. It contributes to less confined bubble lifetime, making bubble more observable by visualization methods. Other point is that the location of bubble formation is fixed, since the laser is focused into a single point, and the variation in the position is almost negligible, considering the straightness of a laser beam.

Chapter 2. Scope of study

2.1. Previous research

The behavior of a single cavitation bubble started from investigating the cause of cavitation damage at the hydro turbomachines. Studying the cause of cavitation damage that is occurring inside rotating machines is still challenging, so research has been conducted on making a single bubble and careful observation has provided the overview of the bubble behavior.

Since the cavitation damage is usually observed on the rotor blades, much early research has focused on the single bubble behavior near rigid boundary. Brujan et al., found that liquid jet is formed at the final stage of the bubble collapse. The jet was toward the rigid boundary, and the intensity of the jet was dependent of the distance between the center of the bubble and the rigid boundary normalized by the maximum bubble radius, which is the stand-off parameter [4]. The same phenomenon has been numerically modelled by Blake et al., via a boundary-integral method. Bubble shapes, and pressure contours have been calculated and showed liquid jet was toward the rigid boundary [5].

The other type of boundary condition, which is the free surface has also been studied by many researchers. Robinson et al., conducted both experiment and numerical calculation to observe the bubble behavior near free surface. The liquid jet was formed at the last stage of the bubble collapse, and it was directed near the free surface. However, the other liquid jet was also found which is away from the free surface [6]. Blake et al., also simulated the same phenomenon with a boundary–integral method, and found that the jet behavior was dependent on the stand–off parameter [7].

The interaction between two boundaries has also been investigated by Gregoricic et al., varying stand–off parameter between two boundaries. As stand–parameter becomes larger than 5, the boundary effects diminished regardless of types of boundaries. They also observed that Rayleigh time, which is defined as the duration between the maximum bubble radius and the final collapse stage, is dependent of the stand–off parameters [8]. The same phenomenon has been numerically simulated by Oguchi et al., who used a moving particle simulation. They showed large deviation from experiment as bubble approached boundaries [9].

To investigate the cause of such jet formation, Obreschkow et al., hypothesized that local pressure gradient would for the

bubble co collapse non-spherically, and conducted experiments. Far from the boundaries, bubble was observed changing the gravitational constant by hyperbolic flight. They found that the liquid jet has the same direction as the local hydrostatic pressure gradient [10]. Without such hydrostatic pressure gradient in case of 0-g flight, bubble showed perfectly spherical behavior throughout entire lifetime. They also conducted experiments varying liquid pressure level, and found that as pressure level decreased the maximum radius of the bubble increased. It has also been simulated by Koukouvinis et al., and the result showed good agreement with the experiment. Without the gravity, bubble showed perfect spherical shape during entire bubble behavior. With gravity, gravity induced jet was simulated. However, the result was too sensitive to mesh, and far field geometry [11].

2.2. Research objectives

Recently, possibilities in high momentum liquid jet for surface cleaning are being considered [12]. This study ultimately aims to verify the possibility of flow control using bubble behavior. More specifically, high divergence during the expansion and jet formation during the final collapse are considered to have high momentum [13]. To use the bubble energy in fluid control, the effect of input energy to create bubble should be investigated. However, accurate control of laser

energy has not been done in previous research. Moreover, numerical simulation for predicting bubble behavior without external source itself is still challenging, and effect of bubble generation method has also not been showing good agreement with the experiment. From the experimental condition, varying the stand-off parameter also changes the plasma structure at the focal point, since the distance between the water-air surface and the focal point gets varied, which is due to different refractive index of water to the air. Therefore, this study is focused on effects of laser pulse energy on bubble behavior far from boundaries at fixed stand-off parameter.

Chapter 3. Experimental setup

3.1. Setup overview

The experimental setup consists of three big components. First, bubble is generated by a pulsed laser. To do the research about a single bubble behavior, only single bubble has to be made on demand. There are two methods, one is to use electrodes in liquid, and the other is to use a pulsed laser. The former case causes geometric confinement to the bubble since electrodes have to be in the liquid. Therefore, pulsed laser has been used to generate a bubble. Second, laser energy has to be controlled precisely. Conventionally, pulsed laser energy is controlled by changing the Q-switching delay of the laser. However, changing

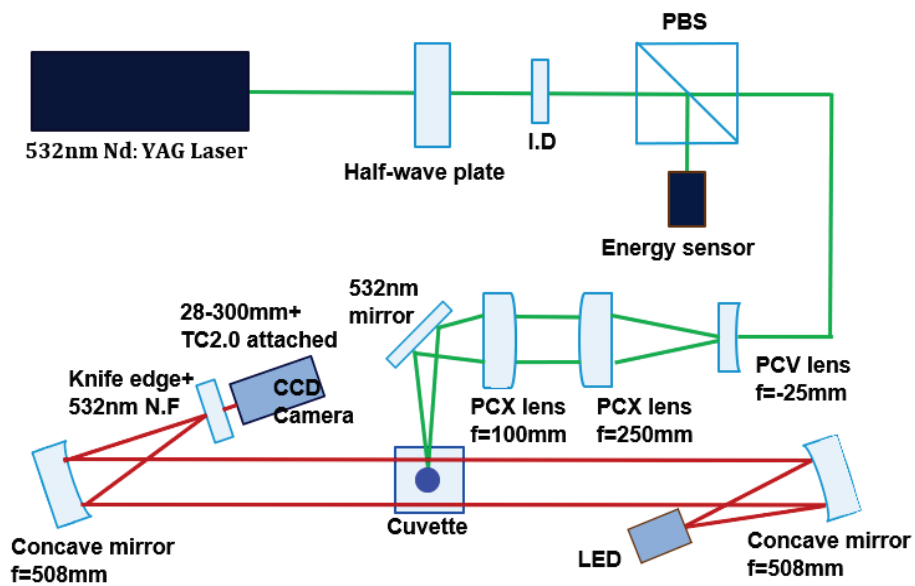


Fig. 3.1 Experimental setup

the Q-switching delay changes laser quality, and hence energy control optics have been used for maintaining laser quality and changing the energy. Lastly, bubble has to be visualized, and a mirror based Schlieren imaging has been chosen.

3.2. Bubble generation

To induce optical breakdown of water, a pulsed laser has to be used. If a continuous laser is used, then the breakdown does not occur, and even if the bubble is made, the process is different. The heating process takes place and it takes much more time to make a bubble. Furthermore, water at the vicinity of a focus point would be heated that precise control of environmental factors is not possible. Therefore, optical breakdown of water was induced by a nanosecond pulsed laser. Nd:YAG pulsed laser (Solo 120, New Wave Research) has pulse width of 6–10ns, and maximum pulse energy of 120mJ.

For the wavelength, 532nm has been chosen which is the second harmonics of Nd:YAG laser. Nd:YAG laser has a fundamental harmonics which is corresponding to 1064nm wavelength. If frequency is doubled, then wavelength becomes the half of 1064nm, which is 532nm. If tripled, wavelength becomes 355nm, and finally if quadrupled, it becomes 266nm. Increasing the frequency not only changes the wavelength of the

laser beam, but also changes the energy level of the beam. The energy of the beam decreases with increasing frequency. From 1064nm to 532nm, energy becomes less than 1/2 of the initial energy. Since the light speed is frequency times the wavelength and considering the loss from the resonator which increases the frequency, at 266nm the energy becomes smaller. However, to have the margin for inducing optical breakdown, choosing 1064nm can cause another problem.

Previous research demonstrates the possibility of creating a cloud of bubbles near the focal point[14]. It is because the infrared absorption of water is much higher than the visible light range. Water molecules are excited by the infrared light since they have nearly the same vibration mode corresponding to the frequency. To observe only single bubble behavior, use of 1064nm(infrared) laser is not recommended. Likewise, use of ultraviolet range for generating bubble is not recommended, either. Considering the water absorption spectrum, ultraviolet range also shows high absorption to water. Another problem regarding absorption spectrum is that laser energy is rapidly absorbed by the water, that only a small partition of initial energy would reach the focal point. As mentioned earlier, energy level of Nd:YAG laser at ultraviolet range already has a lower value than the 1064nm. Therefore, to have a margin for inducing optical breakdown, to avoid generating many bubbles, and to

maintain initial energy level at the focal point, 532nm has been chosen. 532nm range is at the visible range, and the loss due to absorption is the minimum. In addition, since it is visible to naked eye, it helps align or enables to show danger sign during the experiment.

For the peak power, it can yield up to order of MW. However, to induce optical breakdown, laser has to be focused. The focusing lens was tested with a plano-convex lens whose focal length is 75mm. For the current laser, the breakdown did not occur, which means the beam is not focused enough to overcome the threshold. It was due to high divergence of the laser beam. For the test, ablation of solid material was possible with the current laser. Since the breakdown threshold of solid is lower than the liquid, the ablation of solid was observed. It is because the molecule or ion number density of solid is much higher than the liquid, and given the same external energy, more atoms are excited easily.

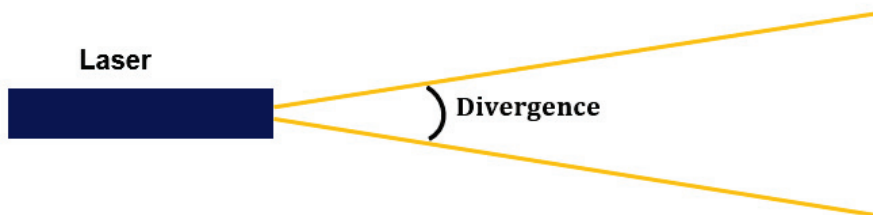


Fig. 3.2 Beam divergence

The laser used in experiment has a divergence of less than 2mrad according to the specification, however, actual measurement result was about 3.7mrad. The measurement has been done by assuming beam diameter is 4.5mm (according to the specification) at the laser exit. Measuring the distance between the laser exit and the target, and calculating the target area, divergence has been estimated. The beam waist radius is approximately linear to beam divergence times the focal length of the focusing lens. Therefore, the higher the divergence of the beam, the larger the waist radius at the focal point. The smaller the focal length of the focusing lens, the smaller the waist radius. Since the energy density has to overcome the optical breakdown threshold of the water, higher divergence or higher focal length is not recommended.

For the test, laser has been focused using a plano-convex lens whose focal length is 75mm at maximum power, but the plasma has not been generated. 75mm focal length was below the minimum considering the Schlieren imaging setup. To overcome the high divergence issue, two solutions have been investigated. One was to use a higher grade focusing lens and the other was to diverge the beam.

The use of higher grade focusing lens could be aspherical lens, or achromatic lens. Even the objective lens could be the

solution. The waist radius becomes smaller as the lens becomes aspherical, since the spherical aberration of the lens becomes smaller than the plano-convex lens. Considering the spherical aberration, achromatic lens has the least waist radius. It is composed of diverging lens and focusing lens. One reduces the divergence and the other aspherical focusing lens focuses the beam. Even the combination of the lens could be the option. The objective lens that is widely used in microscopy is one of such combinations. This lens has much higher focusing ability and are much more expensive. However, considering the beam diameter of 4.5mm, and focal length that is required to be larger than few centimeters to satisfy the far boundaries condition, converging angle becomes too small. This means that before the beam reaches the beam waist, energy density prematurely overcomes the optical breakdown threshold. Therefore, these lenses were not chosen for the experiment.

The other solution is to expand the beam. According to the optics law, at a constant refractive index of a medium where beam is proceeding, divergence of the beam times the beam diameter yields the constant value. This law is widely known and used for calculating beam divergence and focusing ability. Assuming the constant refractive index at the air and water, expanding the beam 10 times reduces the beam divergence by 1/10. Assuming aberration zero lens, which is not possible,

increases the energy density at the waist by 100 times at same energy. This also helps avoid premature overcome of optical breakdown threshold since the converging angle becomes larger.

There are two types of beam expander. One is Keplerian type, and the other is Galilean type. Keplerian type expander uses two focusing lenses for expansion. Initial beam enters lens 1 and focused with a focal length of f_1 . At a distance of f_1 from the lens 1, focal point is seen and the beam passes the point and enters lens 2. Focusing lens 2 makes a beam parallel to the axis of beam. Lens 2 has to be located at a distance of f_2 , which is the focal length of lens 2, from the focal point. It should be noted that focusing lens has a convex inlet for focusing. Lens 1 has a convex shape at the inlet and lens 2 has a convex shape at the exit. Since the focusing lens has a positive focal length, assuming aberration free lenses, beam is expanded by f_2/f_1 . Keplerian type beam expander is widely used for low energy density light. If the energy density is high, then plasma can be formed at the focal point, and the plasma distorts the light path significantly.

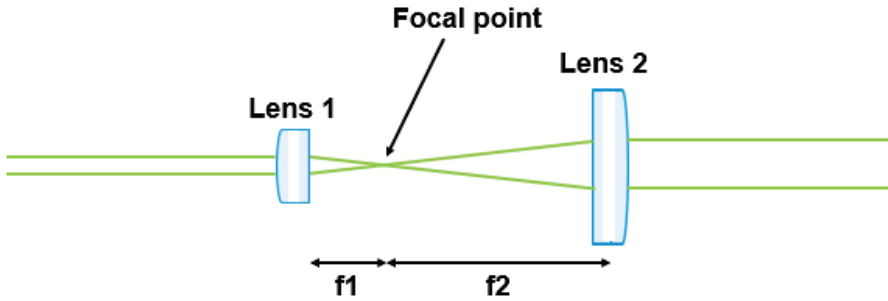


Fig. 3.3 Keplerian type beam expander

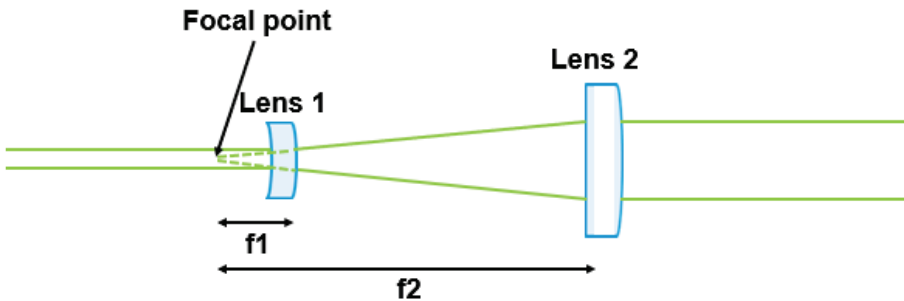


Fig. 3.4 Galilean type beam expander

The other type of beam expander is Galilean type. It has a diverging lens at the inlet and focusing lens at the exit. Initial beam enters lens 1 and expanded. Lens 2 focuses the expanding beam and make it parallel to the axis. Lens 1 has a concave shape at the inlet and lens 2 has a convex shape at the exit. Since the diverging lens has a negative focal length, a focal point is formed in front of the lens at a distance of $-f_1$ which is the focal length of lens 1. To make exit beam parallel to the axis, alignment of lens 2 is significant. Lens 2 has to be located at a distance f_2

from the focal point. Assuming aberration free lenses, beam is expanded by $-f_2/f_1$. Since the focal point is imaginary, which means the beam is not actually focused at the focal point, Galilean type beam expander can be used with high energy density light. Moreover, assuming absolute value of f_1 and f_2 are the same as Keplerian type beam expander, which means the beam is expanded by the same magnification value, axial occupation of lens system is shorter in Galilean type. In case of Keplerian type, axial occupation was f_1+f_2 , however, the sum is only f_2-f_1 for Galilean type. Therefore, Galilean type beam expander has been chosen for beam expansion.

To reduce divergence of the beam, initial beam of 4.5mm diameter was expanded 10 times with a plano-concave lens whose focal length is -25mm . The expanded beam was made parallel with a plano-convex lens whose focal length is 250mm . Neglecting the aberration caused by the lens, focusing expanded beam results in smaller waist radius. However, in reality, every lens has spherical and chromatic aberrations. For the experiment single wavelength which is 532nm has been chosen, so chromatic aberration which is derived from different refractive angle is not significant. However, spherical aberration becomes significant as the beam radius is increased. Usual lens has minimum aberration at the center and as the beam reaches the edge, aberration significantly increases. It can be also found by testing the

distortion from the lens. Images are almost perfect at the center of the lens, however, as the images are seen from the near edges of the lens, they get distorted. To reduce aberration of the lens, oversized lens has been used such that only the center part of the lens would be used for collimation. About 60% of lens radius is used for the collimation, which was suggested by the lens producer.

Since the laser has a divergence, beam diameter at the inlet of beam expander is greater than 4.5mm. Therefore, the beam diameter has to be cut off mechanically. If 5mm beam is expanded 10 times, then beam occupies 60% of 75mm diameter lens. For commercial lens, 75mm is the biggest lens available. The beam was cut off by iris diaphragm which can change diameter from few hundred micrometers to few millimeters. It does not change the divergence of the beam, so it is located just in front of the diverging lens. Since the laser beam is cut off, the energy is decreased after iris, and therefore calibration

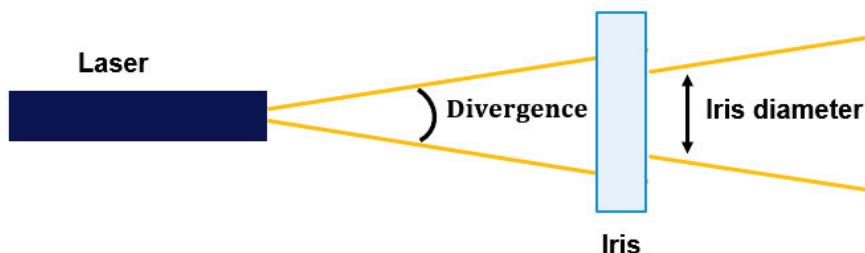


Fig. 3.5 Role of iris

measurement has been performed. The iris diameter was set at 5mm for maximum beam diameter.

For plano-concave lens used for diverging the beam, its diameter is 25mm, beam occupying only 20%. The other lens for collimation, a plano-convex lens has diameter of 75mm. The beam occupies 60%, since the expanded beam diameter is 10 times the 5mm. The final focusing is a plano-convex lens whose focal length is 100mm. The focal length is the minimum considering the Schlieren imaging setup. It has a diameter of 75mm for reducing spherical aberration. After the beam is focused, then it is reflected by 532nm mirror and enters the water. Flat mirror does not change the divergence of the beam, however it can change the wave front of the beam. The surface flatness was chosen for the best beam quality. Expanding and focusing the beam enabled plasma formation only at the focal point. Only a single bubble has been generated and without spending much money on more expensive lenses for expansion and focusing.

3.3. Schlieren imaging

The second part is Schlieren imaging. For visualization, previous research has used high-speed imaging, lens based shadowgraphy, and lens based Schlieren imaging[15–17].

However, direct imaging of a bubble cannot guarantee exact boundary extraction. This is from the lens distortion and camera calibration. Moreover, according to the reference [18], lens based shadowgraphy and Schlieren imaging can cause more aberration than the mirror based ones. Therefore, in this paper, mirror based Schlieren imaging has been used for observing bubble lifetime for the first time.

Diameter of 2 inch mirrors whose focal length of 20 inch have been used, and for illumination, 120W LED has been used. LED has a pinhole assembly in front of the diodes, and 1mm pinhole passes only a fraction of light emitted from the diodes. Light is diverged from the lens system inside the pinhole assembly, and only a fraction of light reaches the first mirror. The mirror focuses the light and makes it parallel. The angle between the optical axis of a diverging light and a parallel light has been aligned to be minimum, ensuring the space for the cuvette. After the light hits the other mirror, it is focused to a knife edge.

For high transmission without distortion in parallel light from the mirror, a cuvette (Quartz 52.5mm x 55mm x 55mm, BSDLab) has been used for water container. It is also more durable to laser than normal glass type cuvette and has more than 90% of transmission, which is suitable for spectroscopy. To prevent any dust and dissolved materials in the water, deionized water has

been used for repeatable experiment.

Just in front of the knife edge, 532nm notch filter of Optical Density(OD) 4 has been used to prevent over-exposure potential to the camera sensor. Over-exposure makes over current in the camera sensor and damages the electronic circuit permanently. Notch filter only reduces the power of beam by a factor of 10^{-4} at 532nm with plus minus 1nm width. For camera, CCD camera(Sensicam QE, Pco) has been used to control exposure and delay to avoid exposure during plasma emission after breakdown. The repetition rate is up to 10fps and considering the bubble lifetime of about few hundred microseconds, images have been taken varying delays after laser shot. Exposure has been set to 500ns for every image at resolution of 1376px by 1040px. Exposure time of 500ns is the minimum that is enabled by the camera and ensures the detection of shock wave underwater after collapse of a bubble.

For imaging lens, it had to satisfy both conditions. One is that it had to have longer focal length as possible for high spatial resolution image of only a few millimeter diameter bubble. However, it also has to be able to focus at 20 inch which is the focal length of the concave mirror. For spatial resolution

calculation, lens maker formula has been used.



Fig. 3.6 Camera lens schematic

$$\text{Field of View} : \text{Working distance} = \text{Sensor size} : \text{Lens focal length}$$

The distance from the center of the cuvette where the laser beam is focused and the Schlieren mirror is about 150mm. The distance has been chosen to be minimum for larger image at the sensor size. Therefore, working distance is about 650mm, since the focal length of the mirror is 20inch. Field of view is about 1mm for maximum bubble diameter. For one pixel of the sensor, horizontal and vertical sizes are the same. The length is 6.45 micrometer. For the spatial resolution, bubble has to be measured with at least 100pixels. Using the equation above, lens focal length is calculated to be 419.25mm. However, there is no lens that has the same focal length. The multi-purpose imaging lens(28–300mm f/3.5–5.6G, Nikon) whose minimum focus length is 50cm has been used. The minimum focus length is the distance between the field of view and the camera sensor.

Therefore, if the minimum focus length is 50cm, then the object can be well captured since the working distance would be smaller than the minimum focal length. Obviously, there are other, but few lenses available for matching two conditions, however, the biggest diameter lens has been chosen for reducing spherical aberration.

After mounting the lens, spatial resolution was 19micrometer per pixel. For better spatial resolution, a teleconver(TELEPLUS PRO 300 2.0X DGX, Kenko) has been used and yielded 12.1 micrometer per pixel. The teleconverter does not change the minimum focal length, and magnifies the image at the value given by the company. It magnifies the image, but it decreases the light entering the lens, thus the light entering the sensor decreases. At 500ns exposure time, additional digital image processing is needed to enhance contrast of the image.

The formula does not always give the correct answer, but it helps estimate the focal length needed for the lens. The image has to be shot and tested, since there are many factors that affect the image size at the sensor. Usually, camera sensor is inside the camera body, and the distance between the sensor and the lens mount is dependent on the lens mount. Moreover, lens focal length in Fig. 3.6 is just a schematic and actual lens has a focal length determined internally.

3.4. Energy control

The last part is laser energy control. Previous research did not require strict control of laser energy since high-speed imaging has been performed for a single laser shot. In this paper, images are being taken with varying delay between a laser shot and camera exposure, laser energy has to be consistent, and controllable. The laser used in this paper is controlled via external triggering. Varying Q-switching delay, pulse energy can be controlled. However, changing Q-switching delay causes pulse energy to fluctuate. At energy level near minimum, the variation in pulse to pulse energy is about 20%, which is not desirable. In addition, parameters that determine the laser quality such as jitter, beam profile, beam divergence, beam pointing stability and beam diameter also degrade as changing Q-switching delay. Therefore, laser is shot at maximum power, which makes laser quality the best and additional optics are added to control the laser pulse energy.

Optics used for controlling laser energy are zero order half wave plate which rotate the polarity of the laser beam and polarizing beam splitter which passes certain polarized beam. Laser beam is linearly polarized and this enables laser to be controlled with changing polarity. Rotating a half wave plate by an angle θ , polarity of a beam is rotated by 2θ . Beam energy

which is proportional to the amplitude of the electric field squared, is cut from polarizing beam splitter by $\cos^2(2\theta + \text{misalignment})$. Rotating the wave plate, the energy measurement has been performed with proper zeroing of the wave plate axis. Energy is monitored by a energy sensor (30(150)A-HE, Ophir) attached to a energy meter (Nova, Ophir) which is able to monitor a single shot. Transmitted beam goes to cavity generation mechanism, and reflected beam goes to the sensor.

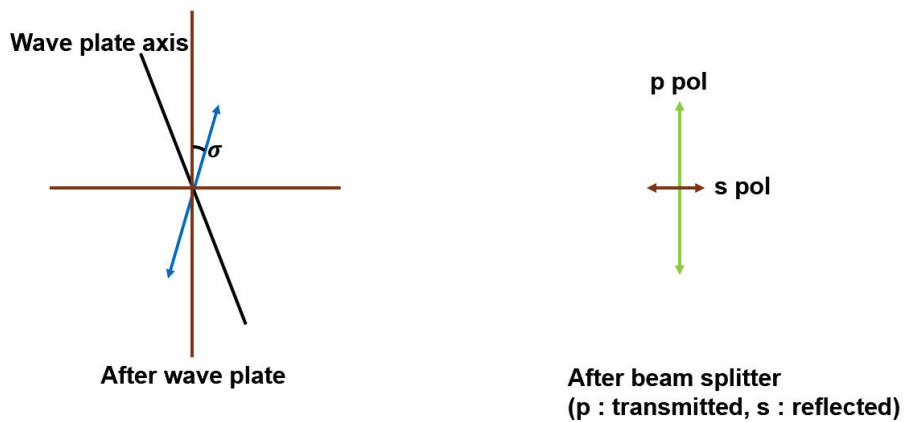


Fig. 3.7 Beam polarity with a wave plate

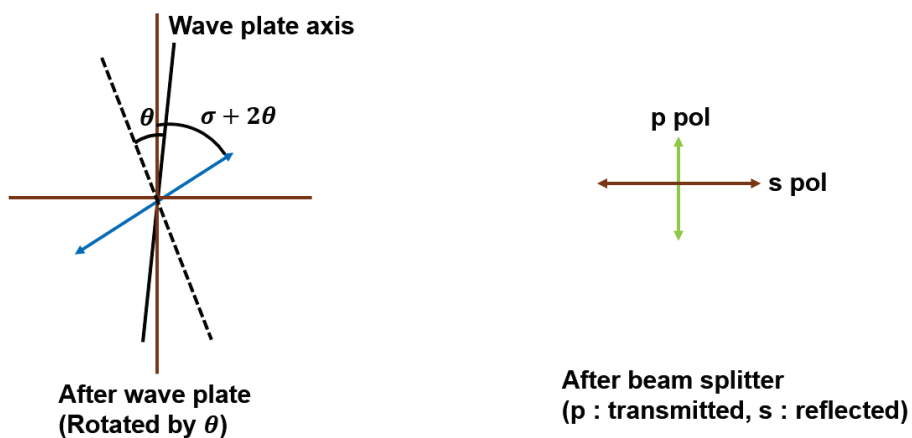


Fig. 3.8 Beam polarity after rotation of wave plate

3.5. Time delay control

Every delay has been made by a pulse generator (9518, Quantum Composer). It controls Q-switching delay of a laser to make maximum pulse energy, and delay between laser shot and camera exposure.

To make a single shot, laser has to be controlled via external trigger. Laser lamp in signal turns on the internal lamp and laser Q switch in signal emits the laser shot. The delay between lamp in and Q switch in is called Q switching delay, and for laser quality the value has been chosen as 190 microseconds. After Q switch in signal, laser is shot after nearly 60 nanoseconds. There is uncertainty in the internal delay of the laser. External delay is triggered by the pulse generator and it varies from 0 to few hundred microseconds. After the external delay, camera in signal is triggered to the CCD camera. Camera has an internal delay which is negligible. After internal delay of the camera, camera exposure starts, and since the exposure has been set at 500ns, image is taken after that and image is obtained. The whole process was repeated 10 times for a single external delay, and external delay increased by 10microseconds until it captures the final collapse.

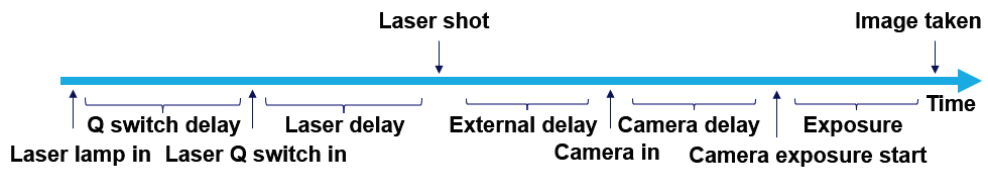


Fig. 3.9 Time domain control

Chapter 4. Results

4.1. Energy measurements

Energy has been measured by a energy sensor (UP19K-15S-VR, Gentec) attached to a energy meter (Tuner, Gentec) at 10Hz. The result is shown in Fig. 4.1. The x axis is the rotation angle of wave plate. The y axis is the measured energy per pulse in mJ. Since the beam splitter splits the beam into transmitted and reflected beam, the measurement has been done for transmitted beam. During the measurement reflected beam has been blocked by the other energy sensor. Blue curve is the theoretical line, and the red circles with error bars are measured points. The error bar has been drawn for sensor and meter uncertainty with approximately 3%. The deviation near the full power comes from the beam splitter loss which is up to 7% of the input energy.

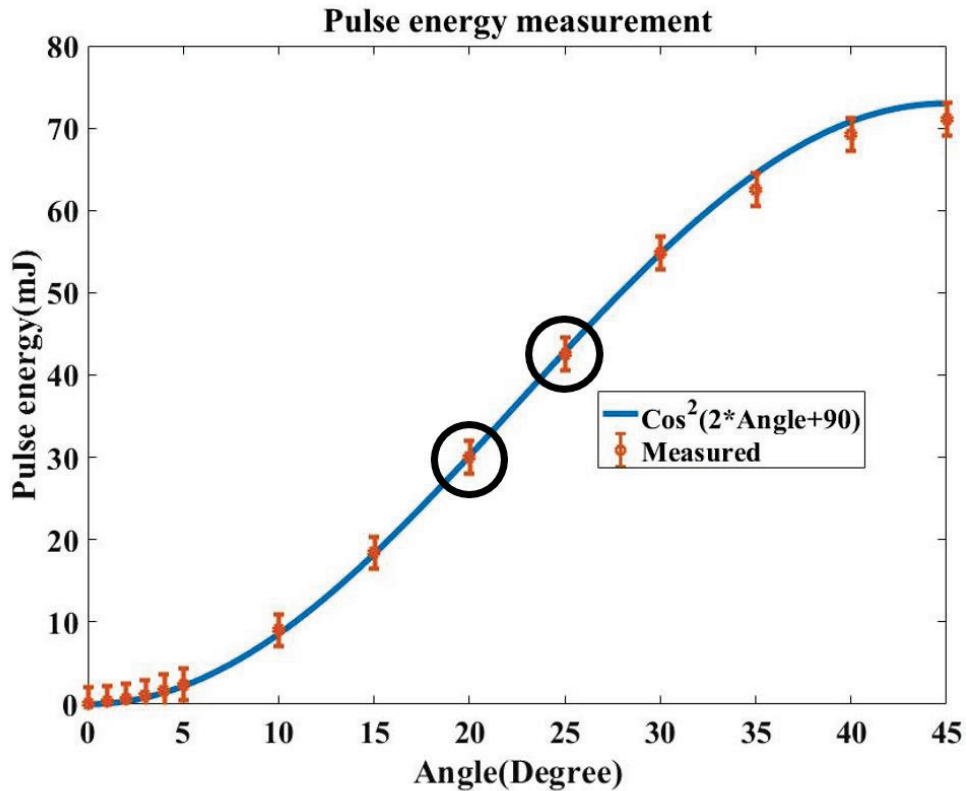


Fig. 4.1 Energy measurements

For the energy values, 30mJ and 42.6mJ have been chosen for the experiment. The threshold for breakdown of tap water was 5mJ, however, deionized water had much higher value of 30mJ. It is thought to rise from dust and dirt in the tap water. Solid has much lower threshold for the breakdown. Solid materials are ionized first, and then surrounding water breakdown occurs after that. At higher energy than 42.6mJ, cuvette started to get damaged from transmission. Therefore, two energy values have been used to generate a bubble.

4.2. Bubble behaviors

Figure 4.2 shows bubble lifetime as delay increases at 30mJ. The bubble initially expands due to energy input from the laser. As bubble expands, water pressure suppresses the growth of a bubble and bubble starts to collapse. This is also a result of adiabatic bubble growth, decreasing inner pressure. As bubble collapses, the interface merges and locally high energy density is achieved. This is emitted as a form of light and shockwave, and only shockwave has been observed. Partial energy is now used for bubble rebound and collapse occurs again. This time, shock is more visible, which means energy dissipation is larger in case of second collapse. After second collapse, bubble expands non-spherically, and due to hydrostatic pressure gradient, liquid jet is formed. After the liquid jet is formed, bubble is collapsed again and diffused into water.

The new discovery from the experiment is that almost spherical rebound after the first collapse has been observed. According to the previous work[19], jet was formed after the first collapse and collapsed again. If the rebound occurred after the second collapse, the overall shape of the bubble was aspherical. Few oscillations after the jet formation, bubble never showed spherical rebound.

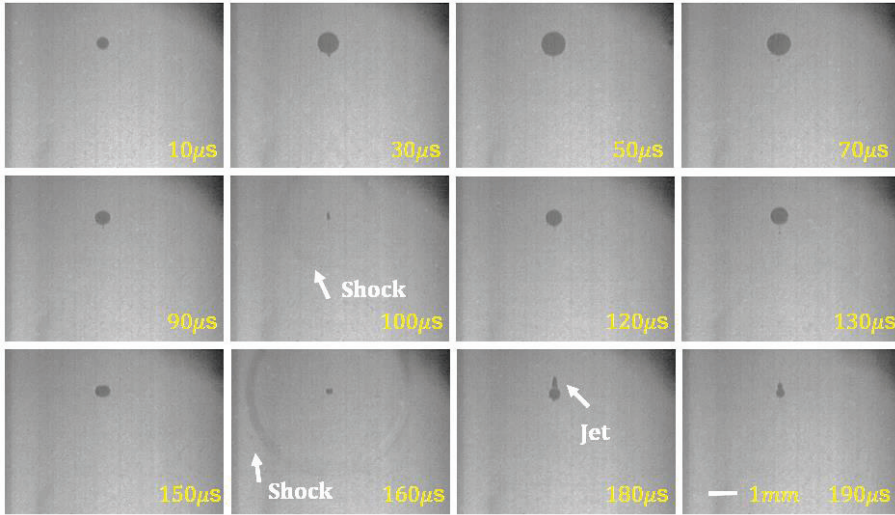


Fig. 4.2 Schlieren images at 30mJ

Figure 4.3 shows the bubble behavior at 42.6mJ. Bubble initially grows and then collapses. After the first collapse, shock is emitted and jet is formed. After the jet formation, bubble collapses again, and does not rebound. The jet formation at the first collapse is similar to previous work. Total duration of growth and collapse for the first time is longer in case of 42.6mJ, and maximum radius of bubble is also larger. The volume of liquid jet is larger in case of 42.6mJ case, too.

Exact delay time is written, and uncertainty in delay is less than 1%. During all measurements, energy has been monitored and showed consistent value within uncertainty. Moreover, water volume stayed constant throughout all measurements, which is crucial for maintaining same pressure level and stand-off parameter. The stand-off parameters for both rigid boundary

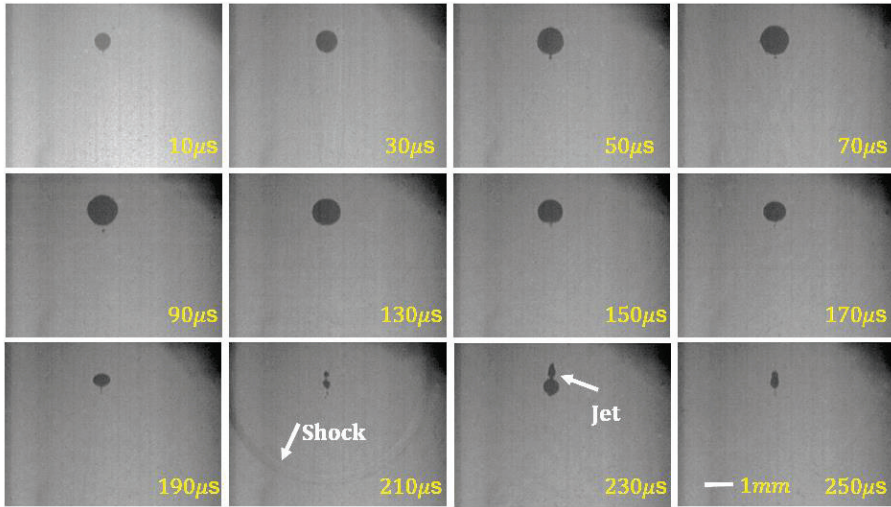


Fig. 4.3 Schlieren images at 42.6mJ

and free surface are larger than 10, which makes the measurement sufficiently far from boundaries. Therefore, the result is explained neglecting boundary effects.

4.3. Discussion: Difference in bubble behaviors

The blue curve in Fig. 4.4 is the Rayleigh solution. The x axis is the time after then laser shot normalized by the Rayleigh collapse time. Rayleigh collapse time is the time the bubble collapses from the maximum size. The y axis is the bubble radius normalized by the maximum radius. Rayleigh equation is the simplest form of Rayleigh–Plesset equation, and numerical solution is drawn. From the Rayleigh equation, numerical result shows that the bubble behavior is symmetric with respect to the time when the bubble becomes the maximum size. Since the Rayleigh equation does not count for non–condensable gas, vapor pressure, surface tension, and temperature effects, only the pressure driven effect is shown.

$$R\ddot{R} + \frac{3}{2}\dot{R}^2 = -\frac{p_\infty}{\rho}$$

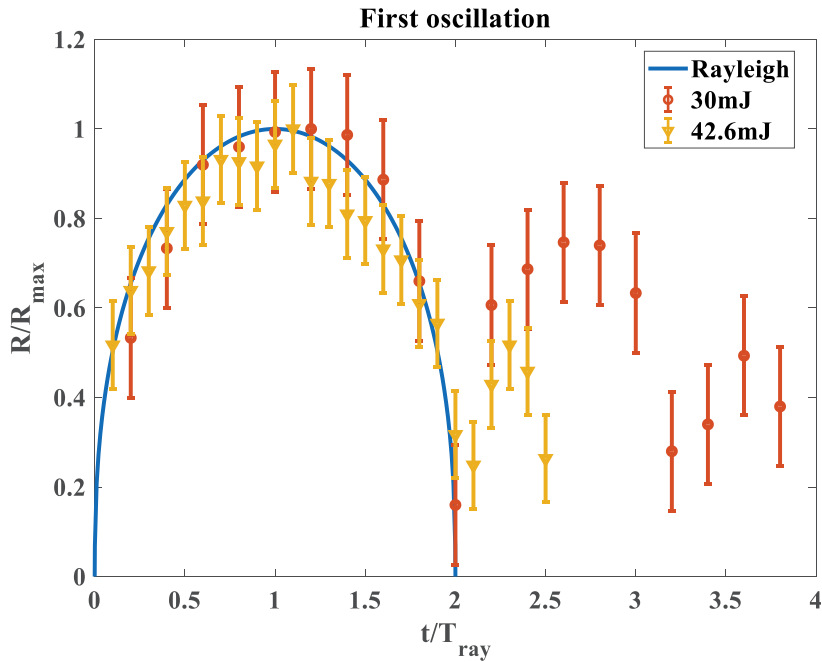


Fig. 4.4 Normalized bubble radius

After the bubble collapses, Rayleigh equation cannot predict the radius of the rebound, so only the experimental results are shown after first oscillation. Red circles are the results from the 30mJ case, and yellow triangles are from the 42.6mJ case. The error bars come from the bubble radius measurement error which was estimated to be 10 pixels. The pixel count corresponds to 0.1mm. There has been much effort to create a bubble repeatedly, however, the result seems that pulse to pulse variation of the laser energy could be high.

For the first oscillation, two experimental results are collapsed into a Rayleigh solution. Therefore, the experiment has

been validated. It means that pressure driven effect is dominant in the first oscillation. The other effects are all neglected, but the two cases are well explained by the pressure effect only.

From the second oscillation, the variation becomes significant. For 30mJ case, the bubble rebounds twice until final collapse, and 42.6mJ case does show only one rebound. The ratio of the rebound radius to the maximum radius is also different. 30mJ case shows larger ratio. Even if in case of 42.6mJ has more energy input, however, more energy fraction is transported to the rebound in 30mJ case. To explain the difference, two key parameters have been introduced.

One is the Weber number (We). Weber number is defined as $We = \frac{\rho \dot{R}^2 R}{\gamma}$. It measures the effect of kinetic energy over surface energy. Since the surface energy tends to make spherical shape, the higher the surface energy is, more spherical the bubble shape becomes. Therefore, the higher the Weber number, more aspherical bubble shapes tend to be shown.

The other is the Bond number (Bo). The Bond number is defined as $Bo = \frac{\Delta \rho g R^2}{\gamma}$. It measures the gravity force over surface tension. Since the liquid jet at the collapse of the bubble is induced by the gravity, it shows the effect of gravity over surface energy. If the effect of gravity is dominant, the bubble shape

would become more aspherical. However, if the surface energy becomes dominant, bubble tends to remain spherical. Therefore, the higher the Bond number, the bubble becomes more aspherical.

Using the Rayleigh equation, the following is obtained analytically.

$$\dot{R} = \sqrt{\frac{2p_{\infty}}{3\rho} \left(\left(\frac{R_{max}}{R} \right)^3 - 1 \right)}$$

Putting in the relation into the Weber number and Bond number, and assuming the same surface tension and gravity and density gradient which is reasonable, the relation becomes

$$We \propto \left(\left(\frac{R_{max}}{R} \right)^3 - 1 \right) \frac{R}{R_{max}} R_{max}$$

$$Bo \propto \left(\frac{R}{R_{max}} \right)^2 R_{max}^2$$

The equations mean that the Weber number and Bond number becomes the function of $\frac{R}{R_{max}}$, R_{max} . The crucial fact from the measurement was that the bubble behavior could be collapsed into a single Rayleigh solution. Therefore, both parameters become the function of R_{max} only. Weber number is linearly proportional to the R_{max} , and Bond number is proportional to the

R_{max} squared. Since the R_{max} was larger in case of 42.6mJ case, both numbers are larger for 42.6mJ case. The change in Weber number and Bond number can be found in the final stage of the first collapse. As can be seen in Fig. 4.5, 42.6mJ case shows more aspherical shape at the final stage of the collapse. This in turn makes the rebound more aspherical and hence the jet formation.

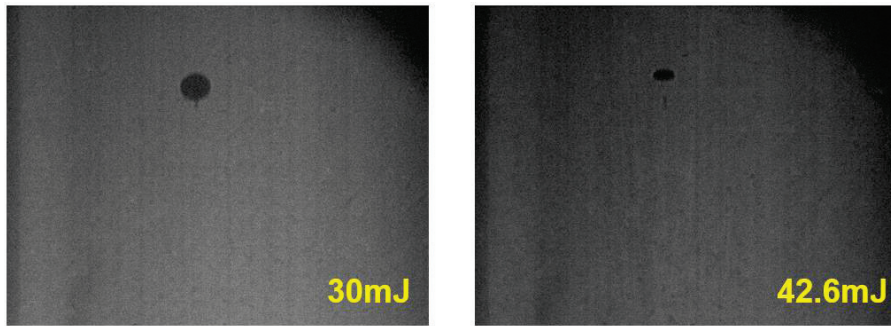


Fig. 4.5 Bubble shape before first collapse(10 microseconds)

The difference in the behavior can be also obtained from the energy analysis. Bubble energy is defined as $E_{bubble} = \frac{4\pi}{3} R_{max}^3 p_{\infty}$.

For the 30mJ case, 1.04% of the laser beam energy is transformed into the bubble energy. During the first rebound, 41.63% of the bubble energy is used from the initial bubble energy. The rest is dissipated into the form of shockwave, noise and light. In case of 42.6mJ, 1.87% of the laser beam energy is transformed into the bubble energy, and the rebound used only 13.82%. The less fraction of the energy means more energy has

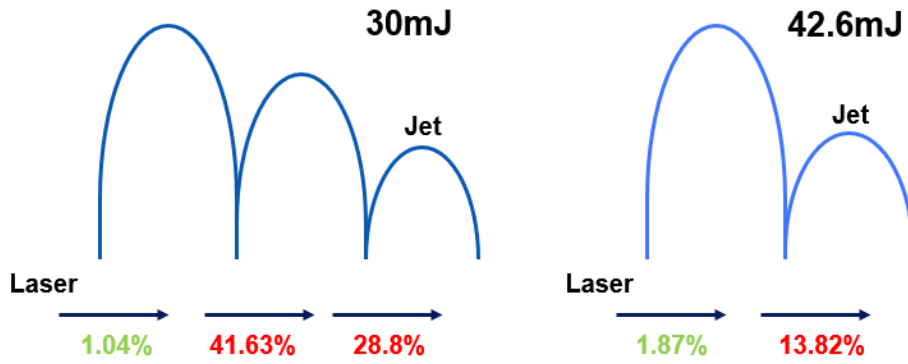


Fig. 4.6 Energy partition for both cases

been lost in the form of shockwave, noise and light. It also means that the surface energy worked more to make the bubble spherical and the effect is the loss of the bubble energy. This can be confirmed by the jet formation at the first rebound, which is due to the gravity.

Back to the 30mJ case, 28.8% of the bubble energy has been used to the second rebound. During the second rebound, jet is formed since the initial energy cannot withstand the effect of gravity. At the first rebound, bubble had energy enough to maintain expand spherically even at the gravity is pushing the boundary. To scale the volume of the jet, the theory has been adopted from the reference [20].

The kinetic energy of the jet is

$$\begin{aligned}
 E &= \int_0^{R(t)} \int_{S(t)} |d\vec{F} \cdot d\vec{R}| \\
 &= \int_0^{R(t)} \int f R^3 |\nabla p \sin\theta \cos\theta| d\varphi d\theta dR
 \end{aligned}$$

The angle θ is the polar angle. The equation is from the assumption that the jet is at the z axis.

$$\begin{aligned}
 &= 2\pi |\nabla p| \int_0^R f R^3 dR, \text{ where } f \propto \frac{R}{R_{max}} \\
 &\propto |\nabla p| R_{max}^4
 \end{aligned}$$

The kinetic energy is also from the definition,

$$E \propto mv^2$$

where

$$v \propto \sqrt{\frac{p_\infty}{\rho}}$$

$$m \propto \frac{|\nabla p| R_{max}^4 \rho}{p_\infty}$$

v is the spatially averaged jet velocity and m is the jet mass.

Assuming the jet volume is the function of the energy partition,

$$V_{jet,max}\rho = \left(\frac{R_{max,rebound}}{R_{max}}\right)^3 m$$

$$V_{nor} = \frac{V_{jet,max}}{\frac{4\pi}{3}R_{max,rebound}^3} \propto \frac{|\nabla p|R_{max}}{p_\infty}$$

The normalized jet volume becomes the function of R_{max} at the same experimental condition. The proportionality factor was interpolated varying pressure level (p_∞), liquid and gravity (∇p). The factor was 5.4 from the research.

For the 30mJ case, the proportionality factor for the normalized jet volume for the second rebound jet was 1123. For the 42.6mJ case, the value for the normalized jet volume for the first rebound jet was 1275. The result exceeded the previous result, however, the two values are similar. The difference is thought to derive from the insufficient temporal resolution of the measurement. The similar values seem to mean the universality of the jet formation.

Chapter 5. Conclusions

Laser pulse energy has been controlled via a half wave plate and polarizing beam splitter. The accurate control in laser pulse energy has not been done for bubble generation research. This reduced the pulse to pulse energy variation, beam profile fluctuation at the focus, and enhanced the stableness of the location of the focus. The method enabled imaging series of bubbles at different delays.

Mirror based Schlieren imaging of bubble lifetime has been conducted for the first time. Shockwave speed in water is order of 2000m/s, the thick front could be detected well. To observe the bubble far away, teleconverter plus zoom lens could be used. The method has not been used for observation of the bubble.

Normalized bubble lifetime far from boundaries for first oscillation collapsed to a Rayleigh solution. This means the first oscillation is explained by the pressure effect.

At 30mJ, spherical rebound at the first rebound has been observed for the first time. To explain the result, Weber number and Bond number have been introduced. Explanation itself is new, and could analyze the spherical rebound from the energy analysis. The exact values for generating the spherical rebound at the first

rebound could not be obtained, however, smaller radius which means linearly smaller Weber number and Bond number squared, could be the main constant.

At 30mJ case, spherical rebound at the first rebound did not result in jet but the second rebound resulted in jet. However, the normalized jet volume from the both cases matched and this means there is universality for the jet.

Bibliography

- [1] Brennen, C. E., 2011, *Hydrodynamics of pumps*, Cambridge University Press.
- [2] Sato, T., Tinguely, M., Oizumi, M., and Farhat, M., 2013, "Evidence for hydrogen generation in laser- or spark-induced cavitation bubbles," *Applied Physics Letters*, 102(7), p. 074105.
- [3] Lam, J., Amans, D., Chaput, F., Diouf, M., Ledoux, G., Mary, N., Masenelli-Varlot, K., Motto-Ros, V., and Dujardin, C., 2014, "gamma-Al₂O₃ nanoparticles synthesised by pulsed laser ablation in liquids: a plasma analysis," *Phys Chem Chem Phys*, 16(3), pp. 963–973.
- [4] Brujan, E. A., Keen, G. S., Vogel, A., and Blake, J. R., 2002, "The final stage of the collapse of a cavitation bubble close to a rigid boundary," *Physics of Fluids*, 14(1), pp. 85–92.
- [5] Blake, J. R., Taib, B. B., and Doherty, G., 2006, "Transient cavities near boundaries. Part 1. Rigid boundary," *Journal of Fluid Mechanics*, 170(-1), p. 479.
- [6] Robinson, P. B., Blake, J. R., Kodama, T., Shima, A., and Tomita, Y., 2001, "Interaction of cavitation bubbles with a free surface," *Journal of Applied Physics*, 89(12), pp. 8225–8237.
- [7] Blake, J. R., Taib, B. B., and Doherty, G., 2006, "Transient cavities near boundaries Part 2. Free surface," *Journal of Fluid Mechanics*, 181(-1), p. 197.
- [8] Gregorčič, P., Petkovšek, R., and Možina, J., 2007, "Investigation of a cavitation bubble between a rigid boundary and a free surface," *Journal of Applied Physics*, 102(9), p. 094904.
- [9] Oguchi, K., Enoki, M., and Hirata, N., 2015, "Numerical Simulation

for Cavitation Bubble Near Free Surface and Rigid Boundary," *Materials Transactions*, 56(4), pp. 534–538.

[10] Obreschkow, D., Kobel, P., Dorsaz, N., de Bosset, A., Nicollier, C., and Farhat, M., 2006, "Cavitation bubble dynamics inside liquid drops in microgravity," *Phys Rev Lett*, 97(9), p. 094502.

[11] Koukouvinis, P., Gavaises, M., Supponen, O., and Farhat, M., 2016, "Numerical simulation of a collapsing bubble subject to gravity," *Physics of Fluids*, 28(3), p. 032110.

[12] Verhaagen, B., and Fernandez Rivas, D., 2016, "Measuring cavitation and its cleaning effect," *Ultrason Sonochem*, 29, pp. 619–628.

[13] Reuter, F., and Mettin, R., 2016, "Mechanisms of single bubble cleaning," *Ultrason Sonochem*, 29, pp. 550–562.

[14] Kovalchuk, T., Toker, G., Bulatov, V., and Schechter, I., 2010, "Laser breakdown in alcohols and water induced by $\lambda=1064\text{nm}$ nanosecond pulses," *Chemical Physics Letters*, 500(4–6), pp. 242–250.

[15] Ohl, C.-D., Arora, M., Dijkink, R., Janve, V., and Lohse, D., 2006, "Surface cleaning from laser-induced cavitation bubbles," *Applied physics letters*, 89(7), p. 074102.

[16] Supponen, O., Kobel, P., Obreschkow, D., and Farhat, M., 2015, "The inner world of a collapsing bubble," *Physics of Fluids*, 27(9), p. 091113.

[17] Martí-López, L., Ocaña, R., Piñeiro, E., and Asensio, A., 2011, "Laser Peening Induced Shock Waves and Cavitation Bubbles in Water Studied by Optical Schlieren Visualization," *Physics Procedia*, 12, pp. 442–451.

[18] Settles, G. S., 2012, *Schlieren and shadowgraph techniques: visualizing phenomena in transparent media*, Springer Science & Business Media.

[19] Petkovšek, R., and Gregorčič, P., 2007, "A laser probe measurement of cavitation bubble dynamics improved by shock wave detection and compared to shadow photography," *Journal of Applied Physics*, 102(4), p. 044909.

[20] Obreschkow, D., Tinguely, M., Dorsaz, N., Kobel, P., de Bosset, A., and Farhat, M., 2011, "Universal scaling law for jets of collapsing bubbles," *Phys Rev Lett*, 107(20), p. 204501.